Nanoscale Res Lett (2010) 5:1962–1969
DOI 10.1007/s11671-010-9733-8

NANO EXPRESS

Hydrothermal Synthesis, Microstructure and Photoluminescence of Eu^{3+}-Doped Mixed Rare Earth Nano-Orthophosphates

Bing Yan · Xiuzhen Xiao

Received: 19 April 2010 / Accepted: 5 August 2010 / Published online: 18 August 2010

Abstract Eu^{3+}-doped mixed rare earth orthophosphates (rare earth = La, Y, Gd) have been prepared by hydrothermal technology, whose crystal phase and microstructure both vary with the molar ratio of the mixed rare earth ions. For $La_xY_{1-x}PO_4$: Eu^{3+}, the ion radius distinction between the La^{3+} and Y^{3+} is so large that only $La_{0.9}Y_{0.1}PO_4$: Eu^{3+} shows the pure monoclinic phase. For $La_xGd_{1-x}PO_4$: Eu^{3+} system, with the increase in the La content, the crystal phase structure of the product changes from the hexagonal phase to the monoclinic phase and the microstructure of them changes from the nanorods to nanowires. Similarly, $Y_xGd_{1-x}PO_4$: Eu^{3+}, $Y_{0.1}Gd_{0.9}PO_4$: Eu^{3+} and $Y_{0.5}Gd_{0.5}PO_4$: Eu^{3+} samples present the pure hexagonal phase and nanorods microstructure, while $Y_{0.9}Gd_{0.1}PO_4$: Eu^{3+} exhibits the tetragonal phase and nanocubic micromorphology. The photoluminescence behaviors of Eu^{3+} in these hosts are strongly related to the nature of the host (composition, crystal phase and microstructure).

Keywords Mixed rare earth orthophosphate · Nanophosphors · Europium ion · Hydrothermal synthesis · Microstructure · Photoluminescence

Introduction

Nanostructure materials with controlled chemical composition, crystal phase structure, morphology and particle size have been extensively investigated during the past few decades because of their high surface/volume ratio and the special quantum confinement effect [1, 2]. Nanomaterials can show remarkable tunable properties and play an important role as active components in the preparation of nanoscale electronic, optical, optoelectronic, electrochemical and electromechanical devices [3–7]. Herein, the fabrication of nanomaterials with well-controlled dimensionality, morphologies, phase purity, chemical composition and desired properties remains one of the most challenging issues [8]. One simple solution to control the particle size and morphology is soft chemistry routes and in particular the hydrothermal process, which is extensively employed in the synthesis of rare earth ions activated inorganic compounds, such as yttrium vanadate, lanthanum fluoride, lanthanum phosphate and yttrium oxide [9–11].

Because of their excellent luminescent properties, rare earth orthophosphates have been extensively applied as phosphors, laser hosts, heat resistant materials and moisture sensors, whose crystal structure and synthesis technology have been studied long time ago [12, 13]. For example, $LaPO_4$: Ce, Tb phosphors have been used as green emission component of tri-chromatic luminescent lamp [14, 15]. Presently, it is important to synthesize rare earth orthophosphate phosphors with regular morphology, composition and size. Ever since Meyssamy et al. has fabricated $LaPO_4$: Eu and $LaPO_4$: Tb nanocrystals by a simple hydrothermal method, lots of works have been focused on the study of rare earth phosphate nanocrystals [16–27]. The crystal structure of pure $LnPO_4$ compounds can be changed with the decrease in Ln ionic radius: i.e., the orthophosphates structure from Ho to Lu as well as Y only exist in the tetragonal zircon (xenotime) structure, while the lanthanide orthophosphates structure (Ln = La ~ Dy) exist in the hexagonal structure under hydrothermal treatment [28]. Mixed orthophosphates composed of two rare earth elements have also been investigated, indicating that these

B. Yan (✉) · X. Xiao
Department of Chemistry, Tongji University,
200092 Shanghai, China
e-mail: byan@tongji.edu.cn

phosphates can be used as host lattices for spectroscopic investigations [29–35].

For $REPO_4$ phosphor of light RE^{3+} with larger ion radius, the monoclinic crystal phase structure is preferred. For $REPO_4$ phosphor of middle RE^{3+} with intermediate radius, a partly hydrated hexagonal structure is favorable. For $REPO_4$ phosphor of heavy RE^{3+} with smaller radius, a tetragonal crystal phase is adopted. Therefore, it is very interesting that what will happen when rare earth ions with different radii are introduced into one $REPO_4$ systems with PO_4^{3-}. In this text, we have investigated the crystal phase structures, microstructure (morphology and particle size) of the mixed orthophosphates $REPO_4$ (RE = La, Gd, Y) prepared by a facile hydrothermal technology. Because of the difference in ion radii between these rare earth ions, the crystal phase and microstructure of the products show obvious differences. At the same time, Eu^{3+} ions have been doped in the mixed rare earth phosphates in order to examine the influence of the hosts on the luminescence of Eu^{3+}, whose photoluminescent behaviors are studied in detail.

Experimental Section

Synthesis of the Mixed Orthophosphates

The starting materials La_2O_3, Y_2O_3, Gd_2O_3 and Eu_2O_3 are firstly dissolved into concentrated nitric acid, and the appropriate volume of deionized water was added to form the 0.2 mol l^{-1} $RE(NO_3)_3$ (RE = Y, La; La, Gd; Y, Gd) and 0.02 mol l^{-1} $Eu(NO_3)_3$, respectively. Then, the mixed orthophosphates doped with Eu^{3+} nanophosphors are synthesized by the hydrothermal process, which are described in the following: the different volume of $Y(NO_3)_3$, $La(NO_3)_3$ ($Gd(NO_3)_3$, $La(NO_3)_3$; $Y(NO_3)_3$, $Gd(NO_3)_3$) and $Eu(NO_3)_3$ (1:0.05 in molar ratio) solutions are mixed with appropriate amounts of $NH_4H_2PO_4$ to form the emulsion. The final pH value is adjusted to 3.0 with HNO_3 solution (1 M). After being stirred, the milky colloid precursor is obtained, suggesting that the nanoscale particle formation already occurred. In order to make the products to crystallize well, the milky colloid precursor is poured into closed Teflon-lined autoclaves to be treated by hydrothermal process (pressure 2.8 MPaG, 0Cr18Ni9Ti stainless steel outdoor shell, 25 mL, safe temperature 200°C, Peking University Qingniao Company, China) at 160°C for 3 days. The resulting product is filtered, washed with deionized water and absolute alcohol to remove ions possibly remaining in the final products $Y_xLa_{1-x}PO_4$: 5% Eu^{3+}, $La_xGd_{1-x}PO_4$: 5% Eu^{3+}, $Y_xGd_{1-x}PO_4$: 5% Eu^{3+}, respectively, ($x = 0.1, 0.5, 0.9$) and finally dried at 60°C in air for further characterization.

Physical Characterization

The X-rays powder diffraction (XRD) patterns of all samples are performed on a Bruke/D8-Advance with Cu$K\alpha$ radiation ($\lambda = 1.540$ Å), whose operation voltage and current are maintained at 40 kV and 40 mA, respectively. Transmission electron microscopic (TEM) images are obtained on a JEOL 2010 microscope with an accelerating voltage of 200 kV. The excitation and emission spectra are recorded with RF-5301 spectrophotometer (resolution used in the excitation and emission spectra measurement is 1 nm). All spectra are normalized to a constant intensity at the maximum. Luminescence lifetime measurements are carried out on an Edinburgh FLS920 phosphorimeter using a 450 W xenon lamp as excitation source. A Netzsch thermoanalyzer, STA 409, is used for simultaneous thermal analysis combining the thermogravimetry (TG) and differential scanning calorimetry (DSC) with a heating rate of 10°C min^{-1}.

Results and Discussion

Crystal Phase and Microstructure of Mixed Rare Earth Phosphates

Li et al. have studied the crystal phase structure of the mixed rare earth phosphates, indicating that pure $LaPO_4$ and YPO_4 crystallize in monoclinic phase and tetragonal phase, respectively, while the mixed phosphate of $La_{0.5}Y_{0.5}PO_4$ belongs to the hexagonal phase [36]. However, the crystal phase structure of the mixed orthophosphates $Y_xLa_{1-x}PO_4$ ($x = 0.1, 0.5, 0.9$) can be changed with different molar ratio of Y^{3+} to La^{3+}, whose XRD pattern of mixed orthophosphates is shown in Fig. 1a. The change of the XRD pattern for $Y_xLa_{1-x}PO4$ (Fig. 1a) depending on the Y:La molar ratio is well known as analyzed as typical solid solution. With the decrease in yttrium ion content, the tetragonal phase cannot be observed and the monoclinic phase appears. With La^{3+} to Y^{3+} of 9:1 M ratio, the product shows the pure monoclinic phase, just like the pure $LaPO_4$. The final product $La_{0.1}Y_{0.9}PO_4$: Eu^{3+} presents the mixture of hexagonal $LaPO_4$ and tetragonal YPO_4 for they cannot form the solid solution. As for $La_xGd_{1-x}PO_4$ ($x = 0.1, 0.5, 0.9$), the mixed rare earth phosphates $La_xGd_{1-x}PO_4$ ($x = 0.1, 0.5$) have the similar pure hexagonal phase, while $La_{0.9}Gd_{0.1}PO_4$ belongs to the pure monoclinic phase (Fig. 1b). The XRD patterns of the mixed $Y_xGd_{1-x}PO_4$ ($x = 0.1, 0.5, 0.9$) are shown in Fig. 1c. The mixed rare earth phosphates $Y_xGd_{1-x}PO_4$ ($x = 0.1$ and 0.5) show the hexagonal phase with the different peak intensities. On the base of the literatures, the $GdPO_4$ powders in most cases have been reported to have the pure hexagonal phase. Besides, the ion radii of Y^{3+} and

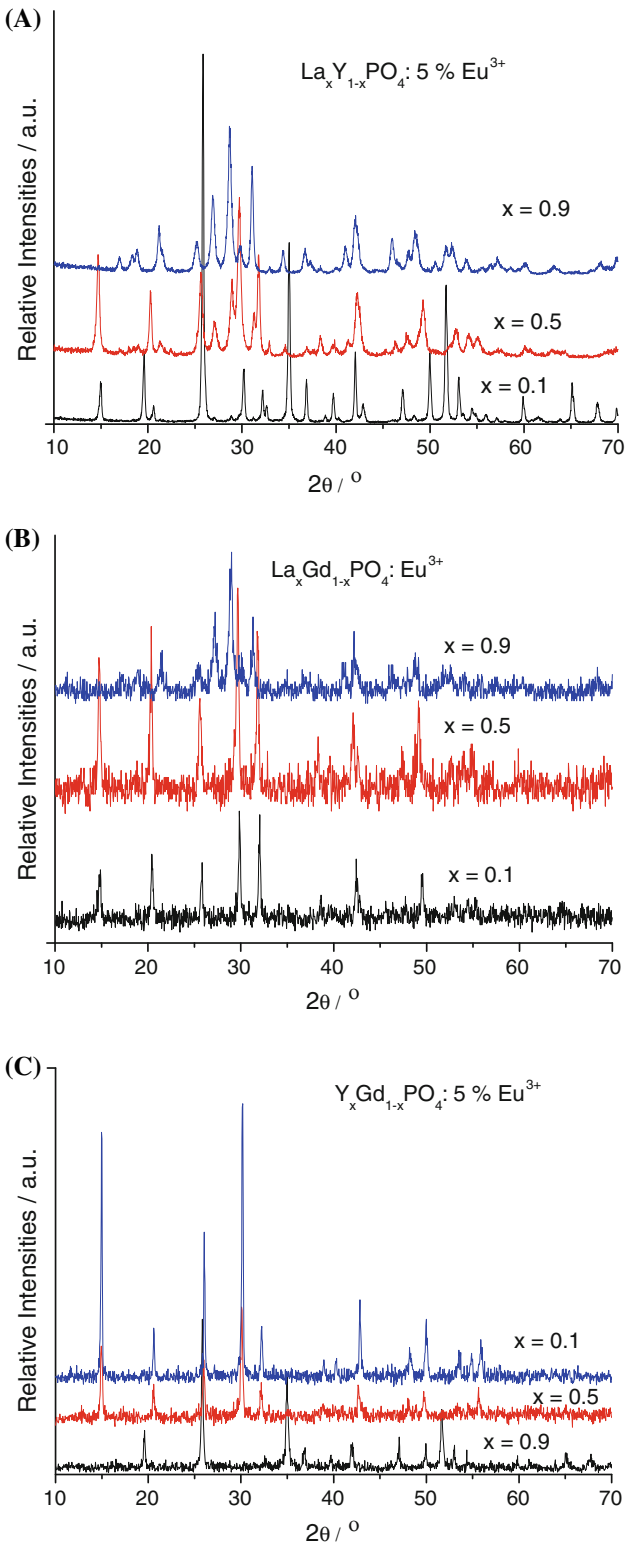

Fig. 1 The XRD patterns of $Y_xLa_{1-x}PO_4$: 5 mol% Eu^{3+} (**a**), $La_xGd_{1-x}PO_4$: 5 mol% Eu^{3+} (**b**) and $Y_xGd_{1-x}PO_4$: 5 mol% Eu^{3+} (**c**) ($x = 0.1, 0.5, 0.9$)

Gd^{3+} are 88 pm and 93.8 pm, respectively, so the replacement of Gd^{3+} by Y^{3+} cannot have an influence on the final crystal phase structure of the product until the content of Y^{3+} reaches 0.9 mol. With the 1:9 M ratio of Gd^{3+} and Y^{3+}, $Y_{0.9}Gd_{0.1}PO_4$ present to the pure tetragonal phase. In one word, because the ion radii of Y^{3+}, Gd^{3+} and La^{3+} are 88, 93.8 and 106.1 pm, respectively, the radii difference between rare earth ions strongly affects the crystal phase and microstructure the mixed rare earth phosphates. The difference in radius between Y^{3+} and La^{3+} is so large that it is not easy to form the product of the single phase. Additionally, the difference in radius between La^{3+} and Gd^{3+} (Gd^{3+} and Y^{3+}) is smaller than that of Y^{3+} and La^{3+}, so the product can present the pure phase with the different content ratio of the rare earth ions. Besides, the calculated grain sizes of these samples are in the range of 12–40 nm using Scherrer's equation, which delegates the dimension in the normal direction of (111) plane.

As for the selected TG curves of the hexagonal mixed rare earth orthophosphates (Fig. 2), there exists the weight loss, which occurs in the range of 150–250°C. This indicates a rapid loss of water molecules from the crystal lattice. Thus, it further proves that the mixed rare earth orthophosphates are hexagonal phase with the hydrated powders. Besides, only a significant weight loss of 6.4 wt% occurred at 165°C and finished at 225°C, approximately corresponding to around 1 mol of H_2O, whose weight loss phenomenon is similar to the report in ref. [35]. Certainly, the existence of water molecule is necessary to stabilize the hexagonal phase [25].

Furthermore, we also have examined the microstructure (particle size and morphology) of the mixed rare earth orthophosphates with the different molar ratio. As shown in Fig. 3, $La_{0.1}Y_{0.9}PO_4$ product (Fig. 3c) is composed with

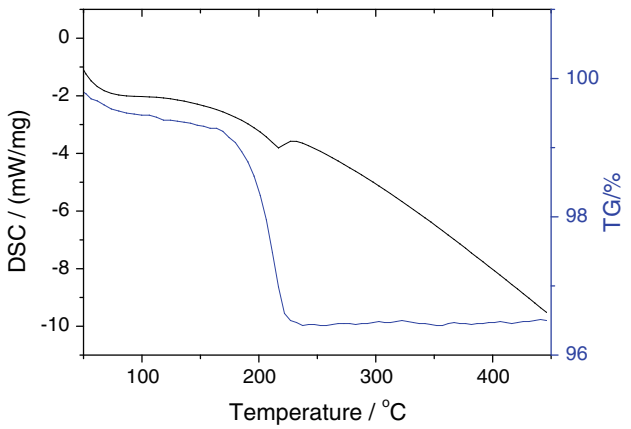

Fig. 2 Selected TG and DSC curves of $Y_{0.5}Gd_{0.5}PO_4$: 5 mol% Eu^{3+}

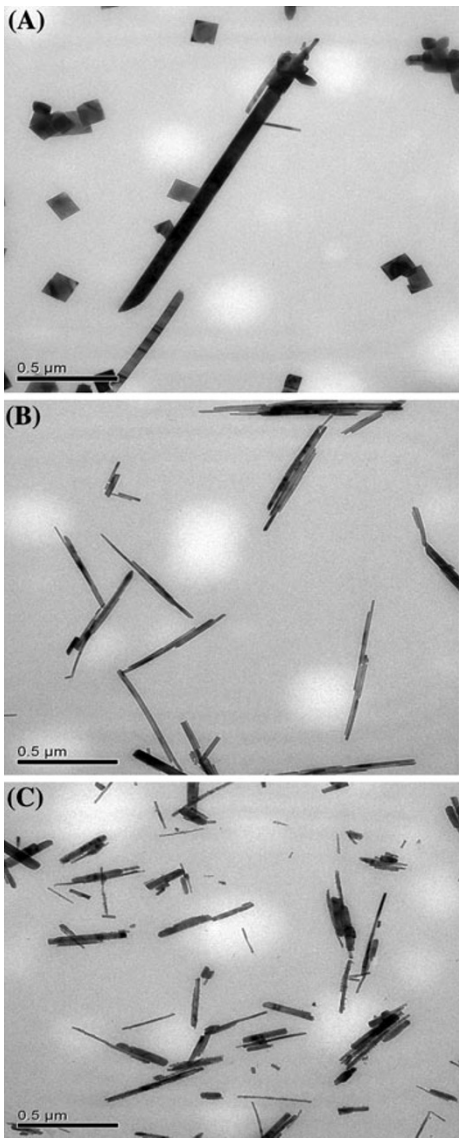

Fig. 3 The TEM pictures of $Y_{0.1}La_{0.9}PO_4$: 5 mol% Eu^{3+} (**a**), $Y_{0.5}La_{0.5}PO_4$: 5 mol% Eu^{3+} (**b**), and $Y_{0.9}La_{0.1}PO_4$: 5 mol% Eu^{3+} (**c**)

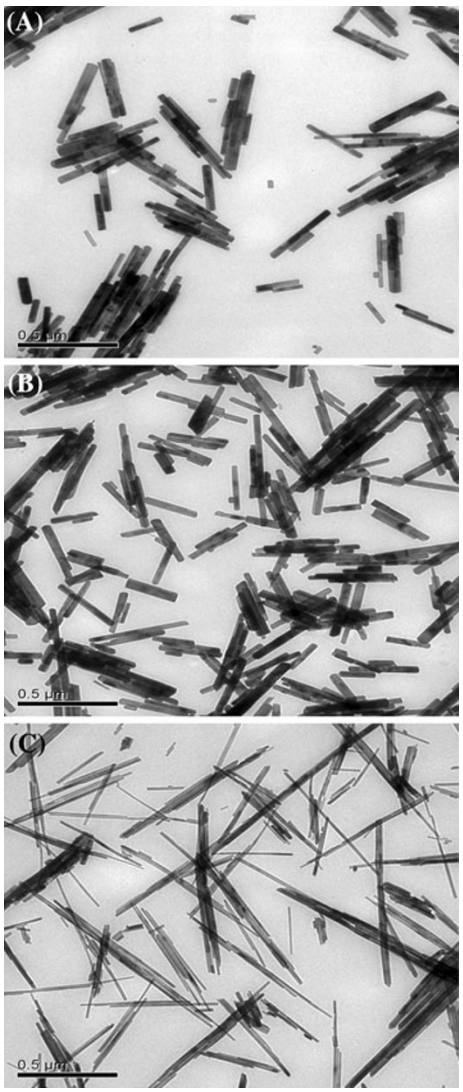

Fig. 4 The TEM pictures of $La_{0.1}Gd_{0.9}PO_4$: 5 mol% Eu^{3+} (**a**), $La_{0.5}Gd_{0.5}PO_4$: 5 mol% Eu^{3+} (**b**), and $La_{0.9}Gd_{0.1}PO_4$: 5 mol% Eu^{3+} (**c**)

the mixed morphologies of the nanoparticles and nanorods (conglomeration of nanowires), which is consistent with the coexistence of the mixed hexagonal and tetragonal phases. Rare earth orthophosphate with hexagonal phase shows a highly anisotropic structure and is favorable for the crystal growth along a certain direction and form the nanorods or nanowires, while it is contrary to the rare earth phosphate with tetragonal structure to form nanoparticles [37, 38]. The actual particle size of these nanophosphors can be estimated to be around 20–80 nm from the measurement of TEM. On the other hand, $Y_xLa_{1-x}PO_4$ samples with hexagonal phase and monoclinic phase are composed of nanowires. Figure 4 shows the TEM images of the mixed orthophosphates $La_xGd_{1-x}PO_4$ ($x = 0.1$, 0.5, 0.9), which presents nanowires or nanorods. With the increase in the La^{3+} content, the ratio of the length to width for the particle is changed. When the molar ratio of Gd^{3+} is higher than 0.5, nanorods is dominated. On the contrary, the nanowires are preferred. However, it needs to be referred that the products present more uniform morphology of nanorods at the molar ratio of Gd^{3+}: La^{3+} of 1:1 than at other molar ratios. The actual particle size of these nanophosphors can be estimated to be around 20–50 nm from the measurement of TEM. Figure 5 shows the microstructure of the mixed orthophosphates $Y_xGd_{1-x}PO_4$ ($x = 0.1$, 0.5, 0.9). Both $Y_{0.1}Gd_{0.9}PO_4$ and $Y_{0.5}Gd_{0.5}PO_4$ show nanorod morphology. The actual particle size of them can be estimated to be around 50–200 nm from the measurement of TEM. Generally, only tetragonal nanocube can be obtained for YPO_4 under such identical conditions,

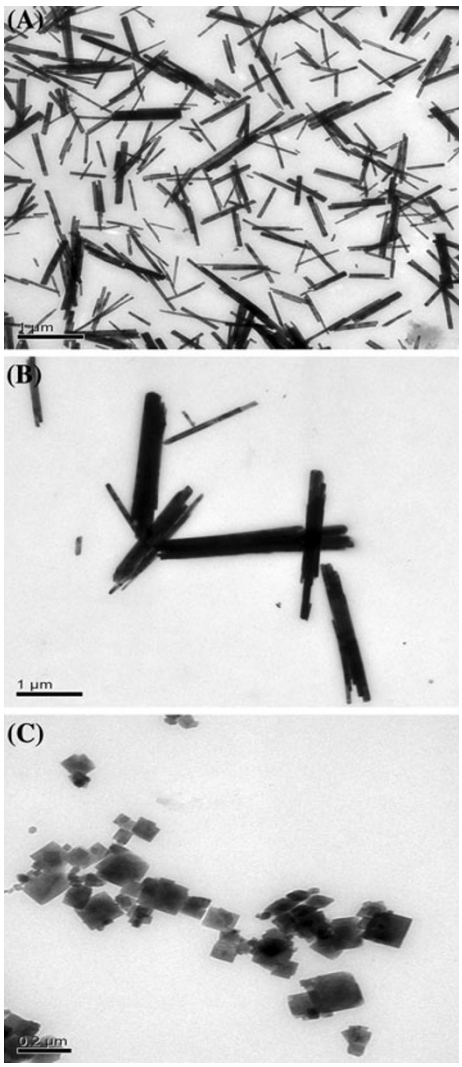

Fig. 5 The TEM pictures of $Y_{0.1}Gd_{0.9}PO_4$: 5 mol% Eu^{3+} (**a**), $Y_{0.5}Gd_{0.5}PO_4$: 5 mol% Eu^{3+} (**b**), and $Y_{0.9}Gd_{0.1}PO_4$: 5 mol% Eu^{3+} (**c**)

which cannot be observed in the TEM images of $Y_{0.1}Gd_{0.9}PO_4$ and $Y_{0.5}Gd_{0.5}PO_4$ products. This is the evidence that we have synthesized $Y_xGd_{1-x}PO_4$ instead of the mixture of YPO_4 and $GdPO_4$. Besides this, tetragonal $Y_{0.9}Gd_{0.1}PO_4$ presents pure nanocube particle. These phenomena are strongly related to the different ratio of the rare earth ions that have the different ion radii.

Generally speaking, the inherent crystal structure determines the crystal growth habitual behavior and final morphology. The hexagonal phase crystal of $Y_xLa_{1-x}PO_4$ commonly appears the anisotropic growth, in which exists apparent layer-like structure along C axle while not along other axles. So it prefers to grow along c axle to release more energy and form the more stable system than other two directions [18, 37, 38]. Finally, $Y_xLa_{1-x}PO_4$ with hexagonal phase will grow to form nanowire or nanorod along [001] direction. On the other hand, the tetragonal phase of mixed orthophosphate does not possess apparent layer-like structure and cannot show the dominated growth direction, resulting in the irregular nanoparticles. For pure monoclinic $La_{0.1}Y_{0.9}PO_4$: Eu^{3+}, crystal structure consists of isolated PO_4 tetrahedron and REO_9-PO_4 chain parallel with c axle. So the crystal still prefers to grow along the [001] direction to make crystal system more stable in spite of that the existence of the chain is not so apparent as layer-like structure of hexagonal phase [18, 37, 38].

Photoluminescent Spectra of Mixed Rare Earth Phosphates

The luminescence of rare earth ions mainly originates from the electron transitions within the 4f shell. However, trivalent Y, La and Lu ions have the empty or completely filled 4f shells, which cannot produce the f–f transitions. Similarly, trivalent Gd^{3+} has a half-filled 4f shell, and the transition energy for f–f transitions of Gd^{3+} is much higher than for other Ln^{3+} with partially filled 4f shells, which is not easy to emit the luminescence too [36]. As a result, the phosphates of these ions are used as host lattice for Eu^{3+}. Herein, we have synthesized the Eu^{3+} activated mixed rare earth phosphates and investigated the luminescence of Eu^{3+} in these hosts. Both excitation and emission spectra of $La_xGd_{1-x}PO_4$ ($x = 0.1, 0.5, 0.9$) are shown in Fig. 6. The excitation spectra consist of a broad band in the short wavelength region and several sharp lines in the long wavelength region. The broad band can be ascribed to the oxygen-to-europium charge transfer band (CTB), whereas the sharp lines correspond to direct excitation of the ground state into higher excited states of the 4f electrons for Eu^{3+}. The position of the CTB of Eu^{3+} in the lattice of hexagonal

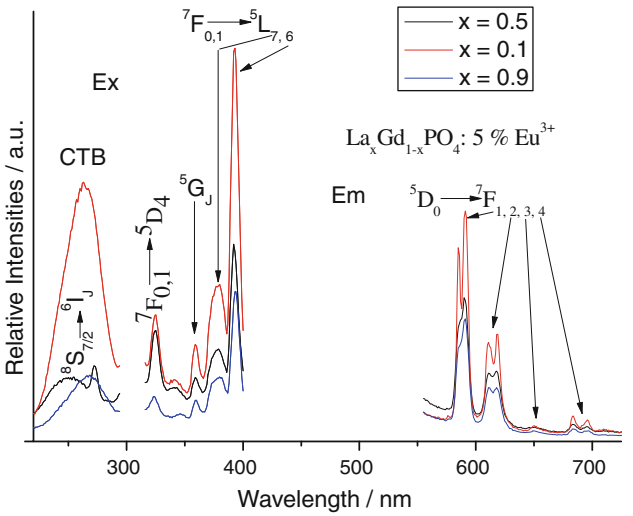

Fig. 6 The excitation (**a**) and emission (**b**) spectra of $La_xGd_{1-x}PO_4$: 5 mol% Eu^{3+} ($x = 0.1, 0.5, 0.9$)

phosphates shifts slightly toward shorter wavelength compared with that in monoclinic $La_{0.9}Gd_{0.1}PO_4$: Eu^{3+} (($_{CTB}$ = 268 nm), being centered at 255 nm for $La_{01}Gd_{0.9}PO_4$: Eu^{3+} and 263 nm for $La_{0.5}Gd_{0.5}PO_4$: Eu^{3+}. This result can be explained by the differences in the Eu–O bond lengths. In the monoclinic rare earth phosphate, RE^{3+} ion is nine-coordinated, while in the hexagonal rare earth phosphate, it is eight-coordinated. This indicates that the average RE–O bond lengths in $La_{0.1}Gd_{0.9}PO_4$: Eu^{3+} and $La_{0.5}Gd_{0.5}PO_4$: Eu^{3+} are shorter than that in monoclinic $La_{0.9}Gd_{0.1}PO_4$: Eu^{3+}. Furthermore, it is observed a new absorption band for $La_{0.1}Gd_{0.9}PO_4$: Eu^{3+}, which peaks at 273 nm. This band is attributed to the $^8S_{7/2}$–^6I_J transitions within Gd^{3+} ions, indicating the occurrence of the energy transfer process from gadolinium ions to europium ones. The emission spectra of $La_xGd_{1-x}PO_4$: Eu^{3+} ($x = 0.1$, 0.5, 0.9) under 393 nm excitation are composed of the characteristic emission lines of Eu^{3+}: $^5D_0$–$^7F_1$, $^5D_0$–$^7F_2$, $^5D_0$–$^7F_3$ and $^5D_0$–$^7F_4$, respectively. The transitions are found to be split into components depending upon the host matrix composition. These phosphors exhibit orange-red color due to the emission transitions $^5D_0$–$^7F_1$ (magnetic dipole line) and $^5D_0$–$^7F_2$ (electric dipole line), respectively. Furthermore, the intensity of the transition $^5D_0$–$^7F_1$ is stronger than that of the transition $^5D_0$–$^7F_2$. As is well known, the relative intensities of $^5D_0$–$^7F_1$ and $^5D_0$–$^7F_2$ emission, which are typical magnetic and electronic dipole–dipole transitions, respectively, depend strongly on the local symmetry of the Eu^{3+} [35–37]. In a site with inversion symmetry, the $^5D_0$–$^7F_1$ magnetic dipole transition is dominating, while in a site without inversion symmetry the $^5D_0$–$^7F_2$ electric dipole transition is the strongest. The results already indicate that more Eu^{3+} occupied the position with the inversion symmetry in host lattices. At the same time, we have found that the intensity of the Eu^{3+} emissions in $La_{0.5}Gd_{0.5}PO_4$ is stronger than that of the other two samples. This can be attributed to the morphology of the $La_{0.5}Gd_{0.5}PO_4$, which presents more uniformity nanorods among these three samples.

For the mixed rare earth phosphate $Y_xGd_{1-x}PO_4$: Eu^{3+} ($x = 0.1$, 0.5, 0.9), both excitation and emission spectra are shown in Fig. 7, which have the similar features to the above. It can be observed the CTB band of O^{2-} to Eu^{3+} (belonging to PO_4^{3-}, here "$^{2-}$" is only the formatted charge of O in PO_4^{2-}), peaking at 253 nm and a sharp absorption band from $^8S_{7/2}$–^6I_J transitions for Gd^{3+}, revealing the existence of the energy transfer process between Gd^{3+} and Eu^{3+}. The characteristic emissions of Gd^{3+} are situated at the strong excitation band of $Y_xGd_{1-x}PO_4$, suggesting that there exists the energy transfer of $Gd^{3+} \rightarrow PO_4^{3-} \rightarrow Eu^{3+}$, at the same time, the energy level difference in ^6G_J and ^6P_J of Gd^{3+} is close to that of $^7F_1$ and $^5D_0$ of Eu^{3+}, a Gd^{3+} in ^6G_J state can excite Eu^{3+} into $^5D_0$ state by resonance energy transfer, which results in the energy transfer of Gd^{3+} to Eu^{3+}

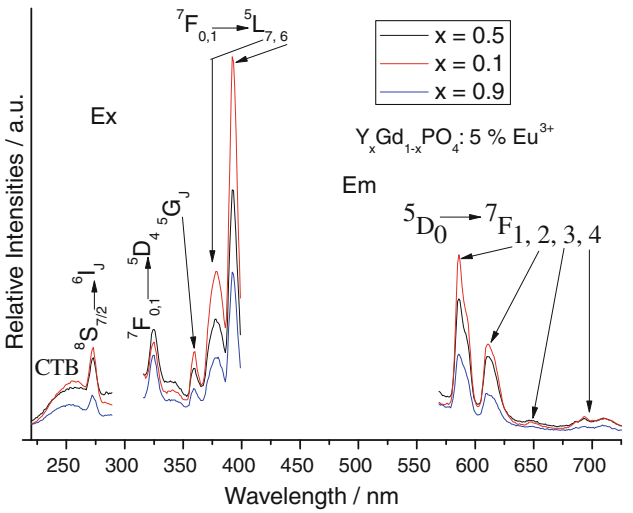

Fig. 7 The excitation **(a)** and emission **(b)** spectra of $Y_xGd_{1-x}PO_4$: 5 mol% Eu^{3+} ($x = 0.1$, 0.5, 0.9)

[39]. Besides this, several strong absorption bands have been observed in the long region of 300–500 nm, which originate from the Eu^{3+} *f–f* transitions. Figure 6B shows the emission spectra of the $Y_xGd_{1-x}PO_4$: Eu^{3+} with the different content ratio of Y^{3+} to Gd^{3+} ions. The characteristic emission can be seen obviously ($^5D_0 \rightarrow {}^7F_J$) originating from low energy transfer of Eu^{3+}. Among these emission lines, $^5D_0 \rightarrow {}^7F_1$ transition is dominant. This indicates that in these hosts, more Eu^{3+} sites are in inversion symmetry. With the content of Gd increases, the intensity of $^5D_0 \rightarrow {}^7F_1$ emission increases. Obviously, Gd^{3+} plays an intermediate role in the energy transfer from PO_4^{3-} to the activator. The energy transfer process in $Y_xGd_{1-x}PO_4$: Eu^{3+} may be described as follows [40]: energy is first absorbed by host absorption band, then is trapped by Gd^{3+} ions and migrated along them until it is trapped by the activator, resulting in the characteristic luminescence. Certainly, Eu^{3+} also can obtain energy from host band directly. Besides, it can be seen the luminescent intensity of $Y_{0.9}Gd_{0.1}PO_4$: Eu^{3+} is weaker than those of other composition, suggesting that the tetragonal phase of $Y_{0.9}Gd_{0.1}PO_4$: Eu^{3+} is not so favorable as the hexagonal phase of $Y_{0.9}Gd_{0.1}PO_4$: Eu^{3+} and $Y_{0.9}Gd_{0.1}PO_4$: Eu^{3+} and the influence of crystal phase on the luminescence is higher than that of water molecules. In addition, either hexagonal phase or tetragonal one cannot show apparent difference in the luminescent intensity of magnetic dipolar transition ($^5D_0 \rightarrow {}^7F_1$) and electronic dipolar transition ($^5D_0 \rightarrow {}^7F_2$).

The photoluminescence spectrum of Eu^{3+} in monoclinic phase $La_{0.9}Y_{0.1}PO_4$ has also been investigated, which is shown in Fig. 8. There are no apparent excitation bands in long wavelength of 300–400 nm and the effective energy absorption takes place in the shorter wavelength of

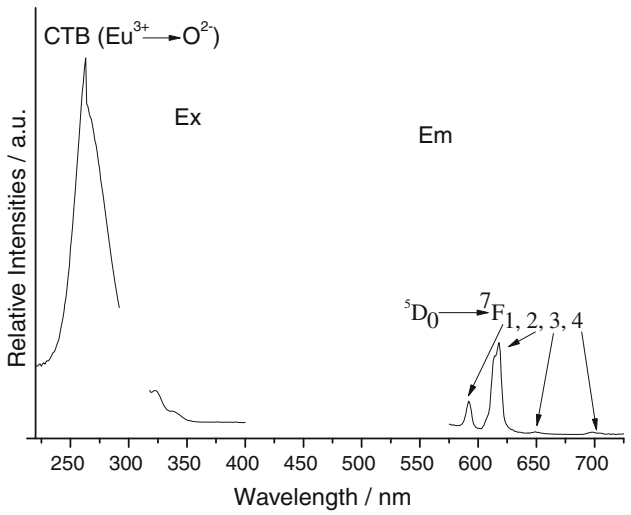

Fig. 8 The excitation **(a)** and emission (**b**) spectra of $Y_{0.1}La_{0.9}PO_4$: 5 mol% Eu^{3+}

Table 1 Photoluminescence lifetimes for $La_xGd_{1-x}PO_4$ Eu^{3+} and $Y_xGd_{1-x}PO_4$: Eu^{3+} Nanophosphors

Nanophosphors	$La_{0.1}Gd_{0.9}PO_4$ Eu^{3+}	$La_{0.5}Gd_{0.5}PO_4$ Eu^{3+}	$La_{0.9}Gd_{0.1}PO_4$ Eu^{3+}
τ (ms)	1.10	3.43	0.85
Nanophosphors	$Y_{0.1}Gd_{0.9}PO_4$ Eu^{3+}	$Y_{0.5}Gd_{0.5}PO_4$ Eu^{3+}	$Y_{0.9}Gd_{0.1}PO_4$ Eu^{3+}
τ (ms)	1.98	1.23	0.38

200–280 nm, peaking at 270 nm. This broad band is ascribed to the CTB band of O^{2-} (belonging to PO_4^{3-}, here "$^{2-}$" is only the formatted charge of O in PO_4^{2-}) to Eu^{3+}. At the same time, under 270 nm excitation, the emission originates mainly from those crystallographic Eu^{3+} sites due to the local energy transfer from Eu–O charge transfer state to the adjacent Eu^{3+} ions. The emission spectra are composed with the characteristic Eu^{3+} emission lines. Different from the luminescent spectra of $Y_xGd_{1-x}PO_4$: Eu^{3+} and $La_xGd_{1-x}PO_4$: Eu^{3+}, the emission intensity of $^5D_0 \rightarrow {}^7F_2$ transition for Eu^{3+} in $La_{0.9}Y_{0.1}PO_4$ is stronger than that of $^5D_0 \rightarrow {}^7F_1$. This result shows that more Eu^{3+} in the monoclinic $La_{0.9}Y_{0.1}PO_4$ occupied the site with less inversion symmetry. When the Eu^{3+} is located at a low-symmetry local site lack of inversion center, the emission at transition is dominated in the emission spectra [41–43]. The resulting lifetime data of the selected Eu-activated rare earth orthophosphates ($La_xGd_{1-x}PO_4$, $Y_xGd_{1-x}PO_4$) are given in Table 1. It can be observed that the composition of hosts with different molar ratio of rare earth ions have great influence on the luminescent lifetimes of excited state of europium ions. Besides, there exists different order between $La_xGd_{1-x}PO_4$: Eu^{3+} and $Y_xGd_{1-x}PO_4$: Eu^{3+}. For $La_xGd_{1-x}PO_4$: Eu^{3+}, the luminescent lifetime reaches the longest (3.43 ms) at the $x = 0.5$, which is much longer than the other two compositions ($x = 0.1$ or 0.9), suggesting there exist a suitable molar ratio of La^{3+} to Gd^{3+} (1:1) for the luminescence of Eu^{3+}. While it is different for $Y_xGd_{1-x}PO_4$: Eu^{3+}, whose lifetime decreases dramatically with the increase in the molar ratio of Y, revealing the introduction of Y ion is not suitable for the luminescence of Eu^{3+}.

Conclusions

In summary, the Eu^{3+} activated rare earth phosphate ($Y_xGd_{1-x}PO_4$, $La_xGd_{1-x}PO_4$ and $Y_xLa_{1-x}PO_4$) nanophosphors ($x = 0.1$, 0.5, 0.9) have been synthesized by hydrothermal technology. The crystal phase and microstructure of the products are strongly depended on the difference in the ion radii of rare earth elements. For Y^{3+} and La^{3+} ions, the difference in the radii is so large that $Y_xLa_{1-x}PO_4$ cannot be favorable for the formation of the pure phase except that $Y_{0.1}La_{0.9}PO_4$ powders present the pure monoclinic phase and nanowires. As for $Y_xGd_{1-x}PO_4$ and $La_xGd_{1-x}PO_4$, the radii difference between two rare earth ions cannot make a big influence on the crystal structure and the morphology. With the increase in the Y content in $Y_xGd_{1-x}PO_4$, the structure of the product has been changed from the hexagonal phase to the tetragonal phase and the morphology from nanorods to nanowires. Similarly, $La_xGd_{1-x}PO_4$ ($x = 0.1$, 0.5) powders have the hexagonal phase and $La_{0.9}Gd_{0.1}PO_4$ belongs to the monoclinic phase. With the increase in the La^{3+} content, the ratio of the length to width has been changed. $Y_{0.1}Gd_{0.9}PO_4$: Eu^{3+} and $La_{0.5}Gd_{0.5}PO_4$: Eu^{3+} nanophosphors present the longest lifetime in the corresponding series. These lanthanide phosphates can be expected to have some potential applications in such fields as fluorescent lamps, plasma display panels and luminescent probes or labels for biomolecule system.

Acknowledgments The work is supported by the Science Fund of Shanghai University for Excellent Youth Scientists and National Natural Science Foundation of China (20971100).

References

1. J.T. Hu, T.W. Odom, C.M. Lieber, Acc. Chem. Res. **32**, 435 (1999)
2. N.I. Kovtyukhova, T.E. Mallouk, Chem. Eur. J. **8**, 4355 (2002)

3. Y. Huang, X.F. Duan, Q.Q. Wei, C.M. Lieber, Science **291**, 630 (2001)
4. M.H. Huang, S. Mao, H. Feick, H. Yan, Y. Wu, H. Kind, E. Weber, R. Russo, P.D. Yang, Science **292**, 1897 (2001)
5. Z.L. Wang, Adv. Mater. **12**, 1295 (2000)
6. C. Dekker, Phys. Today **52**, 22 (1999)
7. S. Frank, P. Poncharal, Z.L. Wang, W.A. de Heer, Science **280**, 1744 (1998)
8. Y.N. Xia, P.D. Yang, Adv. Mater. **15**, 351 (2003)
9. A. Huignard, T. Gacoin, J.P. Boilot, Chem. Mater. **12**, 1090 (2000)
10. A. Huignard, V. Buissette, A.C. Franville, T. Gacoin, J.P. Boilot, J. Phys. Chem. B **107**, 6754 (2003)
11. K. Riwotzki, M. Haase, J. Phys. Chem. B **102**, 10129 (1998)
12. R.C.L. Mooney, J. Chem. Phys. **16**, 1003 (1948)
13. R.C.L. Mooney, Acta Crystallogr. **3**, 337 (1950)
14. J. Dexpert – Ghys, R. Mauricot, M.D. Faucher, J. Lumin. **69**, 203 (1996)
15. M.A. Aia, J. Electrochem. Soc. **114**, 367 (1967)
16. H. Meyssamy, K. Riwotzki, A. Kornowski, S. Naused, M. Haase, Adv. Mater. **11**, 840 (1999)
17. H.T. Shi, L.M. Qi, J.M. Ma, H.M. Cheng, Chem. Commun. **1704**, (2002)
18. Y.P. Fang, A.W. Xu, R.Q. Song, H.X. Zhang, L.P. You, J. Yu, H.Q. Liu, J. Am. Chem. Soc. **125**, 16025 (2003)
19. W.B. Bu, Z.L. Hua, H.R. Chen, L.X. Zhang, J.L. Shi, Chem. Lett. **33**, 612 (2004)
20. Z.G. Yan, Y.W. Zhang, L.P. You, R. Si, C.H. Yan, J. Cryst. Growth **262**, 408 (2004)
21. C.C. Tang, Y. Bando, D. Golberg, R.Z. Ma, Angew. Chem. Int. Ed. **52**, 576 (2005)
22. M.H. Cao, C.W. Hu, Q.Y. Wu, C.X. Guo, Y.J. Qi, E.B. Wang, Nanotechnology **16**, 282 (2005)
23. H. Ito, Y. Fujishiro, T. Sato, A. Okuwaki, Ber. Ceram. Trans. **94**, 146 (1995)
24. R. Kijkowska, R.Z. LeGeros, Key Eng. Mater. **284–286**, 79 (2005)
25. C. Zollfrank, H. Scheel, S. Brungs, P.J. Greil, Cryst. Growth Des. **8**, 766 (2008)
26. Z.A. Peng, X.G. Peng, J. Am. Chem. Soc. **123**, 1389 (2001)
27. Z.A. Peng, X.G. Peng, J. Am. Chem. Soc. **124**, 3343 (2002)
28. Y.W. Zhang, Z.G. Yan, L.P. You, R. Si, C.H. Yan, Eur. J. Inorg. Chem. **4099**, (2003)
29. K. Riwotzki, H. Meyssamy, H. Schnablegger, A. Kornowski, M. Haase, Angew. Chem. Int. Ed. **40**, 573 (2001)
30. K. Riwotzki, H. Meyssamy, A. Kornowski, M. Haase, J. Phys. Chem. B **104**, 2824 (2000)
31. S. Nishihama, T. Hirai, I. Komasawa, J. Mater. Chem. **12**, 1053 (2002)
32. P. Schuetz, F. Caruso, Chem. Mater. **14**, 4509 (2002)
33. D.F. Mullica, E.L. Sappenfield, L.A. Boatner, Inorg. Chim. Acta **244**, 247 (1996)
34. H. Ito, Y. Fujishiro, T. Sato, A. Okuwaki, Br. Ceram. Trans. **94**, 146 (1995)
35. R.X. Yan, X.M. Sun, X. Wang, Q. Peng, Y.D. Li, Chem. Eur. J. **11**, 2183 (2005)
36. M.S. Wickleder, Chem. Rev. **102**, 2011 (2002)
37. W.O. Milligan, D.F. Mullika, G.W. Beall, L.A. Boatner, Acta Crystallogr. **C39**, 23 (1983)
38. W.O. Milligan, D.F. Mullica, G.W. Beall, L.A. Boatner, Inorg. Chim. Acta **60**, 39 (1982)
39. U. Rambabu, S. Buddhudu, Opt. Mater. **17**, 401 (2001)
40. X.Y. Wu, H.P. You, H.T. Cui, X.Q. Zeng, G.Y. Hong, C.H. Kim, C.H. Pyun, B.Y. Yu, C.H. Park, Mater. Res. Bull. **37**, 1531 (2002)
41. Z.L. Wang, H.B. Liang, M.L. Gong, Q. Su, Opt. Mater. **29**, 896 (2007)
42. J.G. Wang, X.P. Jing, C.H. Yan, J.H. Lin, F.H. Liao, J. Lumin. **121**, 57 (2006)
43. M. Yu, J. Lin, Z. Wang, J. Fu, S. Wang, H.J. Zhang, Y.C. Han, Chem. Mater. **14**, 2228 (2002)